Influence of unique layered microstructure on fatigue properties of Ti-48Al-2Cr-2Nb alloys fabricated by electron beam melting

Ken Cho[a], Ryota Kobayashi[a], Jong Yeong Oh[a], Hiroyuki Y. Yasuda[a*], Mitsuharu Todai[b], Takayoshi Nakano[a], Ayako Ikeda[c], Minoru Ueda[d], Masao Takeyama[e]

[a]*Division of Materials and Manufacturing Science, Graduate School of Engineering, Osaka University, 2-1 Yamadaoka, Suita, Osaka 565-0871, Japan*

[b]*Department of Environmental Materials Engineering, Institute of Niihama National College of Technology, 7-1 Yagumo-cho Niihama, Ehime 792-8580, Japan*

[c]*Superalloy Research Group, Research Center for Structural Materials, National Institute for Materials Science, 1-2-1 Sengen, Tsukuba, Ibaraki, 305-0047, Japan*

[d]*Metal Technology Co. Ltd., Harmony Tower 27F, 1-32-2 Honcho, Nakano-Ku, Tokyo, 164-8721, Japan*

[e]*Department of Metallurgy and Ceramics Science, Tokyo Institute of Technology, 2-12-1 Ookayama, Meguro-ku, Tokyo 152-8550, Japan*

*Corresponding author: Hiroyuki Y. Yasuda

Tel.: +81-6-6879-7497

Fax: +81-6-6879-7497

E-mail: hyyasuda@mat.eng.osaka-u.ac.jp

ABSTRACT

The influence of a unique layered microstructure consisting of duplex-like region and equiaxed γ grain layers (γ bands) on the fatigue properties of Ti-48Al-2Cr-2Nb alloy bars fabricated by electron beam melting (EBM) was investigated at room temperature (RT) and 1023 K focusing on the angle (θ) between the building direction and cylinder (loading) axis. We found for the first time the fatigue strengths of the alloy bars with the layered microstructure depend strongly on the angle θ. Particularly, the fatigue strength of the alloy bars fabricated at $\theta = 45°$ is comparable to that of the hot isostatic pressing (HIP) treated cast alloys, even without HIP treatment. We also found the alloy bars fabricated at $\theta = 0°$ and 45° exhibit high fatigue strengths in the low-cycle fatigue life region at 1023 K similar to $\theta = 45°$ alloy bars at RT. These high fatigue strengths are caused by inhibition of the brittle main crack initiation by stress relaxation due to shear deformation at the γ bands and large plasticity of the alloys. These findings indicate that the alloys fabricated by EBM at $\theta = 45°$ with the unique layered microstructure have a great potential for aerospace and automobile applications.

Key words: A. intermetallics (aluminides); B. fatigue resistance and crack growth;

D. microstructure; G. aero–engine components

1. Introduction

Titanium aluminum (TiAl)-based alloys are considered to be prime candidates for aerospace and automobile applications due to their high specific strength, excellent high-temperature (HT) strength and good corrosion resistance [1-3]. Owing to these excellent properties, TiAl-based alloys are expected to partly replace nickel-based superalloys in aero-engine turbine applications with the aim of developing more efficient aero-engines with a high thrust-to-weight ratio [3,4]. In fact, TiAl-based alloys have already been used for low-pressure turbine blades in GEnx engine [5]. However, the poor room temperature (RT) ductility, low HT deformability, and high reactivity of TiAl-based alloys hinder their precise manufacturing. Precision investment casting is the conventional manufacturing process for TiAl-based alloys [6,7]. However, the casting process leads to various problems including coarser grains and shrinkage defects, which in turn results in deterioration in part quality. Moreover, contamination from the crucible and oxidation is significant concerns. To overcome these problems, research is being conducted in two directions. One way is to develop new TiAl-based alloys which can be processed by hot forging [8,9]. For instance, Takeyama *et al*. have suggested the use of a disordered β-phase for the development of wrought TiAl-based alloys [10]. They have developed Ti-Al-Mn [10,11], Ti-Al-V [12,13], Ti-Al-Nb [14], and Ti-Al-M1-M2 (M1, M2: Nb, V, Cr, Mo) [15] alloys. Clemens *et al*. have developed Ti-Al-Nb-Mo-B alloys, which are called TNM alloys [16,17]. These alloys show not only good HT deformability but also high strength at RT as well as HT and good creep properties [13,17]. The second option is to develop new fabrication processes for TiAl-based alloys. Recently, several additive manufacturing techniques, such as electron beam melting (EBM) [18-22] and selective laser melting deposition (SLM) [23-25], have been developed and used to fabricate TiAl-based alloys. It is possible to form complicated shapes without post-processing, to reduce material waste, and to decrease the lead-time using these processes. Especially, EBM has attracted much

attention because of its high energy density and low residual stress as compared to SLM. Recently, Cormier *et al*. [18] and Murr *et al*. [19] have investigated the microstructure of Ti-47Al-2Cr-2Nb (at.%) alloys samples fabricated by EBM. Schwerdtfeger *et al*. [20] have reported an EBM process window for Ti-48Al-2Cr-2Nb (hereafter, referred to as 48-2-2) alloys and the effect of process parameters on the resulting chemical composition. Seifi *et al*. [21] have investigated the effects of hot isostatic pressing (HIP) treatment on microstructures and mechanical properties of 48-2-2 alloys fabricated by EBM. Filippini *et al*. [22] have studied fatigue properties and defect tolerance of 48-2-2 alloys fabricated by EBM. These reports predict that the EBM process is expected to become a next-generation manufacturing system for TiAl-based alloys.

The mechanical properties of TiAl-based alloys are known to depend strongly on their microstructure, which can be controlled by heat treatment [26]. In Ti-rich TiAl alloys, the microstructure generally varies depending on the annealing condition as follows: (i) a fully lamellar structure composed of the TiAl (γ) and the Ti_3Al (α_2) phases, (ii) a duplex structure composed of fine lamellar grains and γ grains and (iii) a near γ structure mainly composed of equiaxed γ grains [26]. For instance, the fine duplex structure is favorable for high strength and good ductility while the coarse fully lamellar structure leads to good creep properties [26].

In our previous study [27], we have reported that it is possible to fabricate cylindrical bars of 48-2-2 alloy by EBM process. Moreover, the alloy bars fabricated with appropriate process parameters have a unique layered microstructure composed of duplex-like region and equiaxed γ grains which form a chain perpendicular to the building direction. These γ grains are referred to as the γ band. The layered microstructure is always aligned perpendicular to the building direction, which is closely related to the temperature distribution around the melt pool during the EBM process [27]. Additionally, it was found that the tensile properties of the alloy bars fabricated by EBM depends strongly on the angle (θ) between the building direction and the

loading axis [27]. At RT, the yield strength of the alloy bars is greater than 550 MPa at all orientations tested of $\theta = 0$, 45, and 90°. In addition, the elongation at $\theta = 45°$ is higher than 2.5% even at RT. This means that the alloy bars at $\theta = 45°$ is more ductile than the cast alloys at RT. Superior RT-ductility of the alloy bars at $\theta = 45°$ is due to the localized shear deformation in the γ bands [27]. These results indicate that the unique layered microstructure is effective to improve tensile strength-ductility balance of 48-2-2 alloys. However, the fatigue properties of additively manufactured 48-2-2 alloy bars containing the unique layered microstructure have not been investigated yet.

In this study, the fatigue properties of 48-2-2 alloy bars fabricated by EBM were evaluated at $\theta = 0°$ and $\theta = 45°$, with a particular focus on the effects of the microstructure and test temperature. Moreover, to investigate the fatigue behavior of the alloy bars, fracture surface and deformation microstructure of specimens after the fatigue tests were observed.

2. Experimental

48-2-2 alloy raw powder used in the present study was fabricated by Ar gas atomization (Arcam AB, Sweden). The average particle diameter of the raw powder is around 100 μm; the chemical composition of the raw powder is listed in Table 1. Cylindrical bars of the 48-2-2 alloy, 10 mm in diameter and 90 mm long, were fabricated using an Arcam A2X EBM system (Arcam AB, Sweden) at an operating voltage of 60 kV. The detail of the fabrication process is well documented in a previous paper [27]. The angle (θ) between the building direction and the cylinder direction of the alloy bars was set at 0° or 45°, as shown in Fig. 1. Hereafter, the alloy bars fabricated at $\theta = 0°$ and at $\theta = 45°$ are referred to as $\theta = 0°$ and $\theta = 45°$, respectively.

The chemical composition of 48-2-2 alloy bars fabricated by EBM was analyzed using an inductively coupled plasma optical emission spectroscopy for metallic elements, an inert

gas fusion method for O and N, and an infrared absorption method for C. The microstructures of the alloy bars fabricated by EBM were observed using an optical microscope (OM) and a scanning electron microscope (SEM). The specimens for OM and SEM observation were mechanically polished using waterproof emery papers of up to #2000 grit and subsequently electrically polished in a $HClO_4$: butanol : methanol (6 : 35 : 59 vol%) solution. Moreover, the specimens for OM observation were etched using a HF : HNO_3 : H_2O (1 : 2 : 97 vol%) etching solution. The local mechanical properties were measured via a nanoindentation hardness test using a nanoindenter at a maximum load of 29.4 mN.

The fatigue properties of 48-2-2 alloy bars fabricated by EBM were evaluated using an electro-servo-hydraulic testing machine. The fatigue tests were conducted at a frequency (f) of 10 Hz at a stress ratio (R) of –1 in the tension-compression mode under a fixed amplitude of the applied stress (σ) at RT and 1023 K in vacuum. The fatigue test specimens of which gauge dimension is $2 \times 2 \times 5$ mm were cut by electro-discharge machining from the center of the alloy bars and then the surface was polished mechanically using waterproof emery papers and a colloidal SiO_2 suspension. It should be noted that the loading axis was set to be parallel to the cylindrical direction during the fatigue tests. The maximum stress amplitude at which the tested specimen does not undergo failure after 1×10^6 cycles (run out) is regarded as the fatigue limit.

The fracture surfaces and side view of fracture parts of the fatigue specimens were carefully observed using SEM. In order to evaluate the localized shear deformation and the dislocation structure during the fatigue tests, the microstructures of the specimens before and after the fatigue tests were analyzed using an electron backscattered diffraction (EBSD) and a transmission electron microscope (TEM). The TEM observations were performed at an accelerating voltage of 300 kV.

3. Results

3.1 Microstructure

The chemical composition of 48-2-2 alloy bars fabricated by EBM is shown in Table 1. Al content decreases by approximately 2 at.% during the EBM process. On the other hand, there is no significant change in Cr and Nb contents. The loss in Al content is caused by evaporation due to its higher vapor pressure as compared to other metallic elements [28]. The C, O, and N contents of the alloy bars fabricated by EBM are comparable to those of the raw powder. This result indicates that contamination during the EBM process is very limited.

Fig. 2 shows the initial microstructure of 48-2-2 alloy bars fabricated by EBM. These OM and SEM images were taken from the cross-section of the bars with respect to the building direction. As shown in Figs. 2 (a) and (b), both $\theta = 0°$ and $\theta = 45°$ show the layered microstructure consisting of the duplex-like region and the γ bands. Figs. 2 (c)–(f) show the high magnification SEM images of the duplex-like region and the γ bands. The duplex-like region consists of lamellar grains, γ grains, and fine α_2 grains (Figs. 2 (c), (d)) while the γ bands are mainly composed of equiaxed γ grains (Figs. 2 (e), (f)). The average grain sizes in duplex-like region (lamellar grains and γ grains) and in γ bands (γ grains) for both $\theta = 0°$ and $\theta = 45°$ is approximately 15 μm and 20 μm, respectively. These grains are much finer than that of the cast alloys with HIP treatment (50–500 μm) [29,30]. Moreover, the width (W_γ) and volume fraction (f_γ) of the γ bands for $\theta = 0°$ are approximately 30 μm and 27%, respectively, and for $\theta = 45°$, the corresponding values are approximately 33 μm and 27%, respectively. This means that the microstructural features of the γ bands in $\theta = 0°$ and $\theta = 45°$ are similar to each other, though the γ bands of $\theta = 0°$ and $\theta = 45°$ are aligned perpendicular to the building direction. These γ bands are formed by repeated local heat treatment in the vicinity of the melt pool during EBM process, which is well described in the previous paper [27].

In order to understand the difference in mechanical properties between the duplex-like region and the γ bands, the nanoindentation tests were done. Fig. 3 shows nanoindentation hardness distribution measured near the duplex-like region/γ band interface in $\theta = 0°$. The nanoindentation hardness of the duplex-like region is much higher than that of the γ bands. Additionally, the hardness varies sharply across the interface between the duplex-like region and the γ band. This is because the duplex-like region contains large amount of the hard α_2 phase. Fine microstructure containing lamellar grains in the duplex-like region also attributes to high hardness. In contrast, the γ grains in the γ bands is coarser than that in duplex-like region. Moreover, in TiAl polysynthetically twinned crystals, the γ phase preferentially deforms [31]. These results indicate that 48-2-2 alloy bars fabricated by EBM have the layered microstructure separated by hard (duplex-like) and soft (γ band) regions.

In addition to the unique microstructure composed of duplex-like region and γ bands, morphology of pores should be also focused on because it is well known that a number of pores are introduced in as-EBM samples [32]. Pores often act as an initiation site of fatigue cracks and play an important role in fatigue failure. Therefore, the shape, diameter, volume fraction (porosity), and distribution of pores in 48-2-2 alloy bars fabricated by EBM were evaluated using OM and SEM. Fig. 4 shows the OM and SEM images of pores in $\theta = 0°$ (Figs. 4 (a), (c)) and $\theta = 45°$ (Figs. 4 (b), (d)). Only circular pores less than 100 μm in diameter could be observed in both $\theta = 0°$ and $\theta = 45°$. The formation of the circular pores are believed to be caused by the atomization gas (Ar) trapped in the raw powder [19,32]. The porosities of $\theta = 0°$ and $\theta = 45°$ are evaluated to be approximately 0.18% and 0.13%, respectively, comparable to that in the previous report (0.1–2.0%) [32]. This indicates that the EBM process parameters used in the present study is optimally adjusted to fabricate the dense 48-2-2 alloy bars. Moreover, as shown in Figs. 4 (c) and (d), the pores are heterogeneously concentrated in the

layered band region. The high-porosity layered regions aligned perpendicular to the building direction can be seen in both $\theta = 0°$ and $\theta = 45°$. The distance between two consecutive high-porosity layered regions is approximately 90 μm, which corresponds to the thickness of the powder layer in each cycle during the EBM process [27]. Therefore, it is supposed that the formation mechanism of the high-porosity layered regions is related to the layer-on-layer process during EBM.

3.3 Fatigue properties

In order to investigate the fatigue properties of 48-2-2 alloy bars fabricated by EBM at $\theta = 0°$ and $\theta = 45°$, fatigue tests were performed under a tension-compression mode at RT and 1023 K in vacuum. Here, it should be noted that the alloy bars fabricated by EBM at $\theta = 0°$ and $\theta = 45°$ were not subjected to HIP treatment. The stress amplitude-number of cycles to failure (S-N_f) curves of $\theta = 0°$ and $\theta = 45°$ cyclically deformed at RT are shown in Fig. 5, along with those of the alloys fabricated by casting followed by HIP treatment [33,34]. At RT, the fatigue strength of $\theta = 0°$ is lower than that of the cast alloys with HIP treatment. On the other hand, the fatigue strength of $\theta = 45°$ at RT, without HIP treatment, is higher than that of $\theta = 0°$ and comparable to that of the cast alloys with HIP treatment. Moreover, the fatigue limits of $\theta = 0°$ and $\theta = 45°$ are approximately 300 MPa and 400 MPa, respectively. These results indicate that the fatigue properties of 48-2-2 alloy bars fabricated by EBM exhibit a strong anisotropy, depending on θ, similar to their tensile properties as reported in ref. [27].

Fig. 6 shows the SEM fractographs of $\theta = 0°$ and $\theta = 45°$ fatigue tested at RT. Note that $\theta = 0°$ and $\theta = 45°$ were cyclically deformed at $\sigma = 400$ MPa and 500 MPa, respectively. Irrespective of θ, the initiation site for the main crack, accompanied with facets, can be observed near the specimen surface (Figs. 6 (a), (b), (d)). Moreover, any defect including pores

cannot be seen around the crack initiation sites. These results indicate that the main crack in both $\theta = 0°$ and $\theta = 45°$ fatigued at RT was not initiated at the pores but at the specimen surface. It is also noted that there is no striation and dimple on the fracture surface of $\theta = 0°$ and $\theta = 45°$, suggesting that the fracture mode is brittle fracture mode. In addition, a number of pores surrounded by facets are observed only on the fracture surface of $\theta = 0°$ (Figs. 6 (a), (c)). In contrast, there is few pores on the fracture surface of $\theta = 45°$. These results indicate that in $\theta = 0°$, small cracks were also initiated at the pores, which influences the crack propagation and fatigue failure at RT. However, in the case of $\theta = 45°$, these negative effects of the pores on the fatigue fracture seem to be negligible.

Fig. 7 shows the side view SEM images of fracture parts of $\theta = 0°$ and $\theta = 45°$ fatigue tested at RT. Note that $\theta = 0°$ and $\theta = 45°$ were cyclically deformed at $\sigma = 400$ MPa and 450 MPa, respectively. The cracks of $\theta = 0°$ and $\theta = 45°$ propagated perpendicular to the loading direction. Moreover, both $\theta = 0°$ and $\theta = 45°$ show smooth crack path. These results also suggest that the fracture mode of $\theta = 0°$ and $\theta = 45°$ is brittle fracture mode. It is also noted that the crack of $\theta = 0°$ propagates in duplex-like region (Fig. 7 (a)). This is because that the duplex-like region is more brittle than the γ bands at RT due to the high hardness (Fig. 3). The crack of $\theta = 45°$ propagates in duplex-like region and passes through the γ bands (Fig. 7 (b)). However, the direction of the crack propagation is not changed at the γ bands. This means that the crack is propagated in the γ bands by transgranular fracture. These results indicate that the crack paths of $\theta = 0°$ and $\theta = 45°$ are less affected by the γ bands or duplex-like region/γ bands interface.

The S-N_f curves of $\theta = 0°$ and $\theta = 45°$ cyclically deformed at 1023 K, along with those at RT are shown in Fig. 8. There is no significant difference in the S-N_f curves between $\theta = 0°$ and $\theta = 45°$ at 1023 K. This means that the anisotropy in the fatigue properties tends to weaken

at 1023 K, which is similar to the tensile properties [27]. In addition, the S-N_f curves can be classified into low- and high-cycle fatigue life regions, which are designated as Regions I and II, respectively. In Region I ($N_f < 1 \times 10^4$ cycles, $\sigma > 450$ MPa), the fatigue strength of $\theta = 0°$ and $\theta = 45°$ at 1023 K is higher than that of $\theta = 0°$ at RT and is comparable to that of $\theta = 45°$ at RT. On the other hand, the slope of S-N_f curves of $\theta = 0°$ and $\theta = 45°$ at 1023 K increase in Region II ($N_f > 1 \times 10^4$ cycles, $\sigma < 450$ MPa), and consequently, the fatigue limit of $\theta = 0°$ and $\theta = 45°$ is approximately 150 MPa. Jouiad *et al*. and Gloanec *et al*. evaluated fatigue properties of the cast alloys with HIP treatment at $R = -1$ under fixed amplitude of total-strain at 1023 K [29,30]. They have reported the cast alloys with HIP treatment are fractured at 200–500 cycles at 1023 K, when $\sigma = 350$–370 MPa. Compared to these reports, it is possible to consider that the fatigue strength of $\theta = 0°$ and $\theta = 45°$ at 1023 K in Region II is comparable to that of the HIP treated cast alloys, even without HIP treatment.

Fig. 9 shows SEM fractographs of the fracture surface of $\theta = 0°$ and $\theta = 45°$ fatigued at 1023 K and then fractured in Region II. Note that σ for $\theta = 0°$ and $\theta = 45°$ is 350 MPa. In contrast to RT, it is difficult to find the clear crack initiation site accompanied with facets on the fracture surfaces at 1023 K (Figs. 9 (a), (b)). The facets can be seen around the pores in both $\theta = 0°$ and $\theta = 45°$ (Figs. 9 (c), (d)). These results indicate that the main and small cracks are initiated at the pores. Thus, unlike at RT, the pores significantly affect the crack initiation, crack propagation and failure in both $\theta = 0°$ and $\theta = 45°$ in Region II at 1023 K. It is also noted that in the γ bands, an intergranular fracture is observed to take place, irrespective of θ (Figs. 9 (e), (f)).

4. Discussion

The fatigue behavior of 48-2-2 alloy bars fabricated by EBM with different θ were

examined through the tension-completion fatigue tests at RT and 1023 K. As a result, it was found that the fatigue behavior at RT exhibited strong anisotropy depending on θ, while that at 1023 K was independent of θ. In addition, the S-N_f curves at 1023 K could be divided into two regions. Thus, the fatigue behavior of 48-2-2 alloy bars fabricated by EBM is discussed focusing on the unique layered microstructure and deformation temperature.

4.1 Fatigue behavior at room temperature

Fatigue strength of as-EBM alloys fatigued at RT was dependent on θ, as shown in Fig. 5. At RT, $\theta = 45°$ demonstrated higher fatigue strength than $\theta = 0°$. Moreover, the fatigue strength of $\theta = 45°$ without HIP treatment was comparable to that of the cast alloys with HIP treatment. In order to understand the anisotropy of the fatigue behavior at RT, plastic strain accumulated in the specimens during the fatigue tests was evaluated. Figs. 10 (a) and (b) show the variation in plastic hysteresis energy (E_p) with σ for $\theta = 0°$ and $\theta = 45°$ at different number of cycles (N) at RT. E_p is defined as the area of the stress-strain hysteresis loop obtained during the fatigue tests and corresponds to the work necessary for the deformation during each cycle [35]. In other words, in the case of stress-controlled fatigue test, higher E_p results in higher plastic strain. E_p of $\theta = 45°$ at RT increases with increasing σ (Fig. 10 (b)), while that of $\theta = 0°$ remains small after 20 cycles (Fig. 10 (a)). Moreover, at $\sigma = 400$ MPa, E_p of $\theta = 45°$ is higher than that of $\theta = 0°$ at any N. These results indicate that the plastic strain of $\theta = 45°$, accumulated during the fatigue tests, is larger than that of $\theta = 0°$. As shown in Figs. 2 and 3, 48-2-2 alloy bars fabricated by EBM have the unique layered microstructure composed of hard (duplex-like region) and soft (γ band) layers. The alignment of the layered microstructure can possibly affect the plastic strain during deformation. For instance, in the tensile tests, the high RT ductility of $\theta = 45°$ is attributed to the localized shear deformation in the soft γ bands [27]. Therefore, during the

fatigue tests, the shear deformation in $\theta = 45°$ is also considered to preferentially occur parallel to the γ bands. In order to examine the strain localization at the γ bands, the specimens cyclically deformed at $\sigma = 300$ MPa and RT were analyzed by EBSD and TEM. Fig. 11 shows the kernel average misorientation (KAM) maps of $\theta = 0°$ (Figs. 11 (a), (b)) and $\theta = 45°$ (Figs. 11 (c), (d)) before and after cyclic deformation to 1×10^5 cycles at RT. KAM of EBSD analysis are known to correspond to the accumulated plastic strain. Note that the observed areas before and after the fatigue tests are exactly the same. In $\theta = 0°$, there is no significant difference in the KAM value before and after the fatigue tests (Figs. 11 (a), (b)). On the other hand, in $\theta = 45°$, the KAM value in the γ band, marked by red circles, increases after the fatigue tests, while no significant change in the KAM is observed in the duplex-like region (Figs. 11 (c), (d)). Moreover, numerous dislocations can be seen in TEM micrographs of fatigued $\theta = 45°$, preferentially in the soft γ bands (Figs. 11 (e), (f)). These results indicate that in contrast to $\theta = 0°$, shear deformation in $\theta = 45°$ easily takes place parallel to the γ bands during the fatigue tests at RT, similar to the tensile tests [27]. Thus, in $\theta = 45°$, the brittle main crack initiation is inhibited by stress relaxation due to the shear deformation along the γ bands. The suppression of the main crack initiation leads to high fatigue strength of $\theta = 45°$ at RT, compared with that of $\theta = 0°$ (Fig. 5). It is also noted that $\theta = 45°$ exhibited higher RT-ductility than the cast alloys with HIP treatment [27]. Consequently, the fatigue strength of $\theta = 45°$ without HIP treatment is comparable to that of the cast alloys with HIP treatment.

Another factor that affects the fatigue properties of 48-2-2 alloy bars at RT is pore formation. As shown in Figs. 11 (a), (b), both the duplex-like region and the γ bands in $\theta = 0°$ did not exhibit any distinct deformation during the fatigue tests at RT. Moreover, E_p of $\theta = 0°$ at RT was very low (Fig. 10 (a)). In this situation, stress concentration around the pores becomes prominent and small cracks are easily initiated at the pores. Additionally, as

described earlier, the pore distribution in both $\theta = 0°$ and $\theta = 45°$ was inhomogeneous as shown in Fig. 4. In $\theta = 0°$, the layers containing large number of pores were aligned perpendicular to the loading axis (Fig. 4 (c)). Therefore, small cracks caused by the pores can easily connect with each other and propagate (Fig. 12 (a)). As a result, the crack propagation rate of $\theta = 0°$ is accelerated at RT, resulting in low fatigue strength (Fig. 5). On the other hand, in $\theta = 45°$, the stress concentration around the pores seems to be weaker than that in $\theta = 0°$ since the shear deformation in $\theta = 45°$ easily occurs along the γ bands (Fig. 11). Thus, small crack initiation at the pores becomes infrequent at $\theta = 45°$. Moreover, the high-porosity layered regions in $\theta = 45°$ were not aligned perpendicular to the loading axis, as shown in Fig. 4 (d). Consequently, the pores in $\theta = 45°$ cannot easily connect with each other (Fig. 12 (b)). Hence, at RT, the crack propagation rate of $\theta = 45°$ is slower than that of $\theta = 0°$, which also contributes to high fatigue strength of $\theta = 45°$.

4.2 Fatigue behavior at 1023 K

In contrast to RT, $\theta = 0°$ and $\theta = 45°$ demonstrated similar *S*-N_f curves at 1023 K (Fig. 8). Figs. 10 (c) and (d) show the variation in E_p with σ for $\theta = 0°$ and $\theta = 45°$ at different N at 1023 K. The relationship between E_p and σ can be divided into Regions I and II, similar to the *S*-N_f curves. As shown in Fig. 8, in Region I, the fatigue strength of both $\theta = 0°$ and $\theta = 45°$ at 1023 K was comparable to that of $\theta = 45°$ at RT. E_p of both $\theta = 0°$ and $\theta = 45°$ in Region I at 1023 K drastically increase with increasing σ (Figs. 10 (c), (d)) and is higher than that of $\theta = 45°$ at RT (Fig. 10 (b)). In addition, 48-2-2 alloys fabricated by EBM exhibit a large elongation above 25 % at 1023 K, regardless of θ [27]. Therefore, the brittle main crack initiation in Region I at 1023 K is inhibited by stress relaxation due to large plastic strains, resulting in high fatigue strength.

On the other hand, the slope of S-N_f curves of both $\theta = 0°$ and $\theta = 45°$ at 1023 K increased in Region II compared with that in Region I (Fig. 8). Here, it should be noted that E_p of $\theta = 0°$ and $\theta = 45°$ in Region II is lower than that in Region I at 1023 K (Figs. 10 (c), (d)). The low plastic strain in Region II leads to an increase in the stress concentration at the pores, which enhances the initiation of the brittle main and small cracks at the pores. Thus, initiation of both cracks at the pores in Region II is more frequent than that in Region I at 1023 K, regardless of θ. It is also noted that in Region II at 1023 K, the small cracks from the pores easily connected with each other and propagated even in $\theta = 45°$ due to the high frequency of the small crack initiation (Fig. 9 (b)). As a result, the crack growth rates of both $\theta = 0°$ and $\theta = 45°$ are accelerated in Region II. Moreover, the intergranular fracture in the γ bands was observed on the fracture surfaces of both $\theta = 0°$ and $\theta = 45°$ at 1023 K (Figs. 9 (e), (f)). This also increases the crack propagation rate, and consequently, increases the slope of S-N_f curves of both $\theta = 0°$ and $\theta = 45°$ in Region II compared with that in Region I.

It is well known that work hardening caused by plastic strain accumulation during cyclic loading can inhibit or retard crack initiation, thus resulting in an increase in the fatigue strength [36,37]. Therefore, in order to examine the effect of work hardening on the fatigue properties, variation in E_p with N for $\theta = 0°$ and $\theta = 45°$ fatigued at RT and 1023 K were compared, as shown in Fig. 13. Note that σ of $\theta = 0°$ (Fig. 13 (a)) and $\theta = 45°$ (Fig. 13 (b)) are 300 MPa and 400 MPa, respectively. E_p of both $\theta = 0°$ and $\theta = 45°$ fatigued at RT decrease rapidly with increasing N. This result indicates that the work hardening associated with the cyclic loading at RT is relatively strong. However, at 1023 K, the decrease in E_p with N becomes small, especially in $\theta = 45°$, compared with that at RT. These results indicate that dynamic recovery occurs during the fatigue tests at 1023 K. In fact, dynamic recovery also takes place in TiAl polysynthetically twinned alloys cyclically deformed at 973 K [38]. Therefore, the work

hardening which was prominent at RT is not significant at 1023 K due to the dynamic recovery. The weak work hardening at 1023 K also leads to the large slope of S-N_f curves in Region II.

Although the slope of S-N_f curves of $\theta = 0°$ and $\theta = 45°$ in Region II is larger than that in Region I at 1023 K, the fatigue strength of these bars in Region II is comparable to that of HIP treated cast alloys, even without HIP treatment. This is because the grain size of $\theta = 0°$ and $\theta = 45°$ (15–20 μm) is finer than that of the cast alloys with HIP treatment (50–500 μm) [29,30].

From the present study, it was found that 48-2-2 alloy bars fabricated by EBM at $\theta = 45°$ not only show a good tensile strength-ductility balance but also high and acceptable fatigue strength at RT and 1023 K, respectively. These excellent mechanical properties are a result of the unique layered microstructure consisting of the duplex-like region and the γ bands. This indicates that the alloys fabricated by EBM at $\theta = 45°$ with the unique layered microstructure have a great potential for aerospace and automobile applications.

5. Conclusions

The fatigue properties of 48-2-2 alloy bars fabricated by EBM at $\theta = 0°$ and $\theta = 45°$ without HIP treatment was examined with a particular focus on the layered microstructure and the test temperature. The following conclusions could be drawn from the present study:

1. At RT, the fatigue strength of $\theta = 0°$ is lower than that of the alloys fabricated by casting followed by HIP treatment. On the other hand, the fatigue strength of $\theta = 45°$ is higher than that of $\theta = 0°$ and comparable to that of the cast alloys with HIP treatment.
2. At 1023 K, the both $\theta = 0°$ and $\theta = 45°$ show high fatigue strength similar to $\theta = 45°$ at RT in the low-cycle fatigue life region. Moreover, in the high-cycle fatigue life region, the fatigue strength of both $\theta = 0°$ and $\theta = 45°$ is comparable to that of the cast alloys with HIP treatment.

3. At RT, shear deformation in $\theta = 45°$ preferentially takes place parallel to the γ bands during the fatigue tests. As a result, the brittle main and small crack initiation is inhibited by the stress relaxation by the shear deformation. Moreover, the small cracks around the pores cannot easily connect with each other and propagate in $\theta = 45°$ since the high-porosity layered regions in $\theta = 45°$ are not aligned perpendicular to the loading axis, which also results in high fatigue strength of $\theta = 45°$ at RT.
4. At 1023 K, E_p of both $\theta = 0°$ and $\theta = 45°$ drastically increases with increasing σ in the low-cycle fatigue life region. As a result, the brittle main crack initiation is inhibited by stress relaxation due to large plastic strains, which results in high fatigue strength in the region.
5. At 1023 K, E_p at both θ in high-cycle fatigue life region is lower than that in low-cycle region. Consequently, in the high-cycle region at 1023 K, the brittle main and small crack initiation at the pores becomes frequent due to the increase in the stress concentration associated with low E_p. Moreover, the occurrence of the intergranular fracture at the γ bands increases the crack propagation rate. Additionally, dynamic recovery occurs during the fatigue tests at 1023 K, which weakens the work hardening. These are the reasons for the large slope of S-N_f curves of $\theta = 0°$ and $\theta = 45°$ at 1023 K in high-cycle fatigue life region.

Acknowledgements

This study was supported by the Cross-Ministerial Strategic Innovation Promotion Program (SIP) “Structural Materials for Innovation” from the Japan Science and Technology Agency (JST).

References

[1] Y.-W. Kim, Ordered intermetallic alloys, part III: Gamma titanium aluminides, JOM 46 (1994) 30–39.

[2] Y.-W. Kim, D.M., Dimiduk, M.H. Loretto, Gamma Titanium Aluminides 1999, Warrendale, PA, TMS (1999).

[3] F. Appel, J.D.H. Paul, M. Oehring, Gamma Titanium Aluminide Alloys, Singapore, Wiley-VCH (2011).

[4] X. Wu, Review of alloy and process development of TiAl alloys, Intermetallics 14 (2006) 1114–1122.

[5] B.P. Bewlay, S. Nag, A. Suzuki, M.J. Weimer, TiAl alloys in commercial aircraft engines, Mater. High Temp. 3409 (2016) 1–11.

[6] J. Aguilar, A. Schievenbusch, O, Kättlitz, Investment casting technology for production of TiAl low pressure turbine blades – Process engineering and parameter analysis, Intermetallics 19 (2011) 757–761.

[7] Y, Dong, D. Zhang, K. Bu, Y. Dou, W. Wang, Geometric parameter-based optimization of the die profile for the investment casting of aerofoil-shaped turbine blades, Int. J. Adv. Manuf. Technol. 57 (2011) 1245–1258.

[8] M. Takeyama, S. Kobayashi, Physical metallurgy for wrought gamma titanium aluminides: Microstructure control through phase transformations, Intermetallics 13 (2005) 993–999.

[9] H. Clemens, S, Mayer, Intermetallic titanium aluminides in aerospace applications – processing, microstructure and properties, Mater. High Temp. 33 (2016) 560–570.

[10] T. Tetsui, K. Shindo, S. Kobayashi and M. Takeyama, A newly developed hot worked TiAl alloy for blades and structural components, Scripta Mater. 47 (2002) 399–403.

[11] T. Tetsui, K. Shindo, S. Kaji, S. Kobayashi, M. Takeyama, Fabrication of TiAl components by means of hot forging and machining, Intermetallics 13 (2005) 971–978.

[12] S. Kobayashi, M. Takeyama, T. Motegi, N. Hirota, T. Matsuo, Microstructure control using β-Ti phase for wrought gamma TiAl based alloys , In: Y.-W. Kim, H. Clemens, A.H. Rosenberger, Gamma Titanium Aluminides 2003, Warrendale, PA, TMS (2003) 165–176.

[13] T. Tetsui, K. Shindo, S. Kobayashi, M. Takeyama, Strengthening a high-strength TiAl alloy by hot-forging, Intermetallics, 11 (2003) 299–306.

[14] M. Takeyama, Y. Kato, M. Kikuchi, Phase equilibria among α, α_2, β and γ phases in ternary Ti-Al-X systems at elevated temperature, In P.A. Blenkinsop, W.J. Evans, H.M. Flower, Proceedings of the 8th World Conference on Titanium (1995) 294.

[15] H. Nakashima, M. Takeyama, Phase stability of β-Ti phase in the TiAl alloys with the combined addition of M elements, MRS Proceedings, 1760 (2015) mrsf14-1760-yy06-07.

[16] H. Clemens, W. Wallgram, S. Kremmer, V. Güther, A. Otto, A. Bartels, Design of novel β-solidifying TiAl alloys with adjustable β/B2-phase fraction and excellent hot-workability, Adv. Eng. Mater. 10 (2008) 707–713.

[17] H. Clemens, S. Mayer, Design, processing, microstructure, properties, and applications of advanced intermetallic TiAl alloys, Adv. Eng. Mater. 15 (2013) 191–215.

[18] D. Cormier, O. Harrysson, T. Mahale, H. West, Freeform fabrication of titanium aluminide via electron beam melting using prealloyed and blended powders, Res. Lett. Mater. Sci. 2017 (2007) 34737–34740.

[19] L.E. Murr, S.M. Gaytan, A. Ceylan, E. Martinez, J.L. Martinez, D.H. Hernandez,B.I. Machado, D.A. Ramirez, F. Medina, S. Collins, R.B. Wicker, Characterization of titanium

aluminide alloy components fabricated by additive manufacturing using electron beam melting, Acta Mater. 58 (2010) 1887–1894.

[20] J. Schwerdtfeger, C. Körner, Selective electron beam melting ofTi-48Al-2Nb-2Cr: microstructure and aluminium loss, Intermetallics 49 (2014) 29–35.

[21] M. Seifi, A.A.Salem, D.P. Satko, Ulf. Ackelid, S.L. Semiatin, J.J. Lewandowski, Effects of HIP on microstructural heterogeneity, defect distribution and mechanical properties of additively manufactured EBM Ti-48Al-2Cr-2Nb, J. Alloys Compd. 729 (2017) 1118–1135.

[22] M. Filippini, S. Beretta, L. Patriarca, G. Pasquero, S. Sabbadini, Defect tolerance of a gamma titanium aluminide alloy , Proc. Eng. 10 (2011) 3677–3682.

[23] B. Cárcel, A. Serrano, J. Zambrano, V. Amigó, A.C. Cárcel, Laser cladding of TiAl intermetallic alloy on Ti6Al4V – Process optimization and properties, Phys. Procedia 56 (2014) 284–293.

[24] L. Löber, F.P. Schimansky, U. Kühn, F. Pyczak, J. Eckert, Selective laser melting of a beta-solidifying TNM-B1 titanium aluminide alloy, J. Mater. Process. Technol. 214 (2015) 1852–1860.

[25] X. Shi, S. Ma, C. Liu, Q. Wu, Parameter optimization for Ti-47Al-2Cr-2Nb in selective laser melting based on geometric characteristics of single scan tracks, Opt. & Laser Technol. 90 (2017) 71–79.

[26] D.M. Dimiduk, D.B. Miracle, Y.W. Kim, M.G. Mendiratta, Recent progress on intermetallic alloys for advanced aerospace systems, ISIJ Int. 31 (1991) 1223–1234.

[27] M. Todai, T. Nakano, T. Liu, H.Y. Yasuda, K. Hagihara, K. Cho, M. Ueda, M. Takeyama, Effect of building direction on the microstructure and tensile properties of Ti-48Al-2Cr-

2Nb alloy additively manufactured by electron beam melting, Additive Manufacturing 13 (2017) 61–70.

[28] H.P. Tang, G.Y. Yang, W.P. Jia, W.W. He, S.L. Lu, M. Qian, Additive manufacturing of a high niobium-containing titanium aluminide alloy by selective electron beam melting, Mater. Sci. Eng. A 636 (2015) 103–107.

[29] M. Jouiad, A.L. Gloanec, M. Grange, G. Henaff, Cyclic deformation mechanisms in a cast gamma titanium aluminide alloy, Mater. Sci. Eng. A 400-401 (2005) 409–412.

[30] A.L. Gloanec, T. Milani, G. Henaff, Impact of microstructure, temperature and strain ratio on energy-based low-cycle fatigue life prediction models for TiAl alloys, Int. J. Fatigue 32 (2010) 1015–1021.

[31] T. Fujiwara, A. Nakamura, M. Hosomi, S. R. Nishitani, Y. Shirai, M. Yamaguchi, Deformation of polysynthetically twinned crystals of TiAl with a nearly stoichiometric composition, Phil. Mag. A, 61 (1990) 591–606.

[32] S. Biamino, A. Penna, U. Ackelid, S. Sabbadini, O. Tassa, P. Fino, M. Pavese, P.Gennaro, C. Badini, Electron beam melting of Ti-48Al-2Cr-2Nb alloy: microstructure and mechanical properties investigation, Intermetallics 19 (2011) 776–781.

[33] T. Kruml, M. Petrenec, K. Obrtlík, J. Polák, P. Buček, Influence of niobium alloying on the low cycle fatigue of cast TiAl alloys at room and high temperatures, Procedia Engineering 2 (2010) 2297–2305.

[34] J.M. Larsen, Assuring reliability of gamma titanim aluminides in long-term service, In: Y.-W. Kim, D.M. Dimiduck, M. Loretto, Gamma Titanium Aluminides 1999, Warrendale, PA, TMS (1999) 463–472.

[35] T. Nakano, H.Y. Yasuda, N. Higashitanaka, Y. Umakoshi, Anomalous behaviour of cyclic deformation and fatigue properties of TiAl PST crystals under constant applied stress, Acta Mater. 45 (1997) 4807–4821.

[36] S. Nishida, C. Zhou, N. Hattori, S. Wang, Fatigue strength improvement of notched structural steels with work hardening, Mater. Sci. Eng. A 468-470 (2007) 176–183.

[37] I.F. Pariente, M. Guagliano, About the role of residual stresses and surface work hardening on fatigue ΔKth of a nitrided and shot peened low-alloy steel, Surf. Coat. Technol. 202 (2008) 3072–3080.

[38] Y. Umakoshi, H.Y. Yasuda, T. Nakano, Effect of deformation temperature on fatigue and fracture behavior in TiAl polysynthetically twinned crystals, Metall. Mater. Trans. A 29A (1998) 943–950.

Table and figure captions

Table

Table 1 Chemical composition of the raw powder and the EBM fabricated cylindrical bar.

Figure

Fig. 1 Schematic drawing of cylindrical bars fabricated by EBM.

Fig. 2 OM and SEM images of $\theta = 0°$ ((a), (c), (e)) and $\theta = 45°$ ((b), (d), (f)); OM images ((a), (b)), SEM images of the duplex-like region ((c), (d)) and the γ band ((e), (f)).

Fig. 3 Nanoindentation hardness distribution in $\theta = 0°$, measured near the duplex-like region/γ band interface.

Fig. 4 OM ((a), (b)) and SEM ((c), (d)) images of pores in $\theta = 0°$ ((a), (c)) and $\theta = 45°$ ((b), (d)).

Fig. 5 S-N_f curves of $\theta = 0°$ and $\theta = 45°$ cyclically deformed at RT, along with that of the cast alloys with HIP treatment.

Fig. 6 SEM fractographs after the fatigue tests at RT. (a), (c) $\theta = 0°$, $\sigma = 400$ MPa, $N_f = 1042$ cycles, (b), (d) $\theta = 45°$, $\sigma = 500$ MPa, $N_f = 151$ cycles. (a), (b) Low magnification images of the fracture surface, (c) a pore surrounded by some facets, (d) crack initiation site of near the specimen surface.

Fig. 7 Side view SEM images of fracture parts after the fatigue tests at RT. (a) $\theta = 0°$, $\sigma = 400$ MPa, $N_f = 1042$ cycles, (b) $\theta = 45°$, $\sigma = 450$ MPa, $N_f = 16378$ cycles

Fig. 8 S-N_f curves of $\theta = 0°$ and $\theta = 45°$ cyclically deformed at 1023 K, along with those at RT.

Fig. 9 SEM fractographs after the fatigue tests at 1023 K. (a), (c), (e) $\theta = 0°$, $\sigma = 350$ MPa, $N_f = 11748$ cycles, (b), (d), (f) $\theta = 45°$, $\sigma = 350$ MPa, $N_f = 11903$ cycles. (a), (b) Low magnification images of the fracture surface. The pores ((c), (d)) and the γ bands ((e), (f)) observed on the fracture surface.

Fig. 10 Variation in E_p with σ for $\theta = 0°$ ((a), (c)) and $\theta = 45°$ ((b), (d)) at RT ((a), (b)) and 1023 K ((c), (d)).

Fig. 11 EBSD KAM maps of $\theta = 0°$ ((a), (b)) and $\theta = 45°$ ((c), (d)) before ((a), (c)) and after ((b), (d)) the fatigue tests at RT; $\sigma = 300$ MPa, $N = 1 \times 10^5$ cycles. (e), (f) TEM bright-field images of dislocation structure in fatigued $\theta = 45°$. (e) The duplex-like region, (f) the duplex-like region/γ band interface.

Fig. 12 Schematic drawing of small crack propagation at $\theta = 0°$ (a) and $\theta = 45°$ (b). Unlike in the case of $\theta = 0°$, small cracks cannot easily connect with each other and propagate in $\theta = 45°$.

Fig. 13 Variation in E_p with N for $\theta = 0°$ (a) and $\theta = 45°$ (b) fatigue tested at RT or 1023 K. (a) $\sigma = 300$ MPa, (b) $\sigma = 400$ MPa.

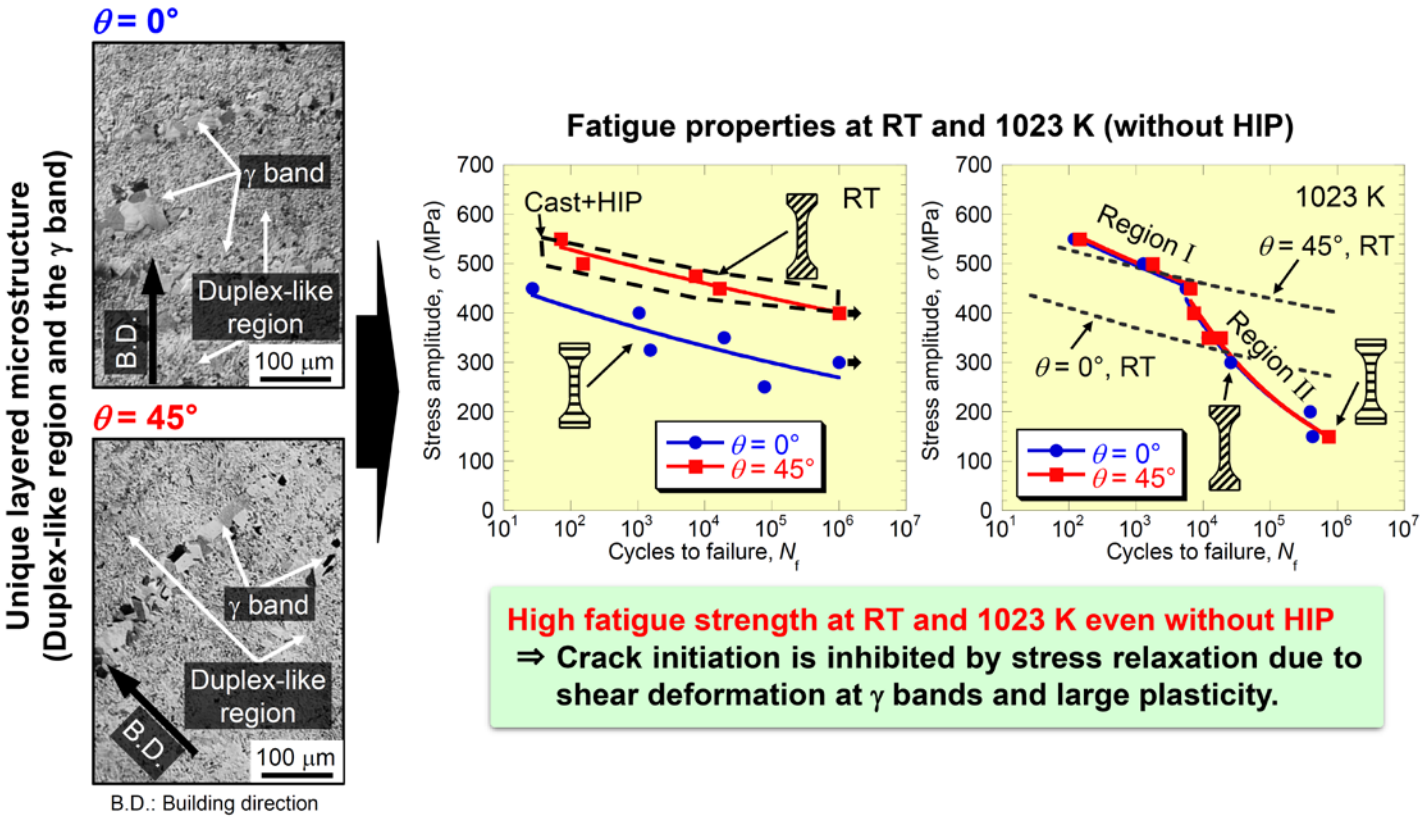

Graphical abstract

Table 1. Chemical composition of the raw powder and the EBM fabricated cylindrical bar.

(at.%)

	Ti	Al	Cr	Nb	C	O	N
Raw powder	Bal.	48.6	1.74	1.95	0.032	0.193	0.008
Cylindrical bar	Bal.	46.3	1.72	2.10	0.049	0.215	0.020

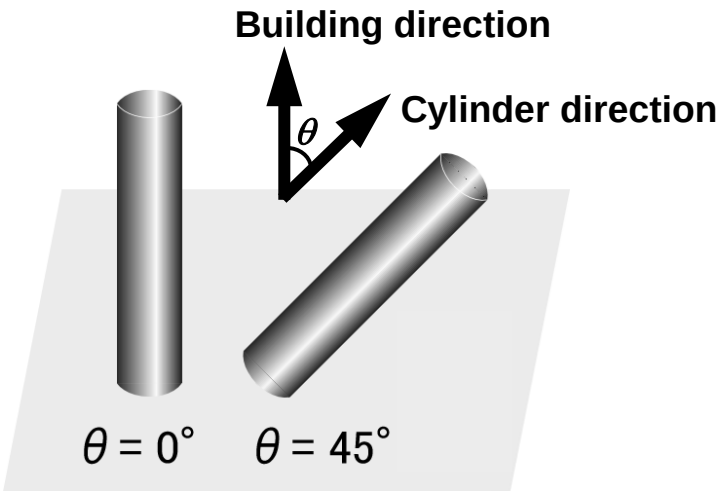

Fig. 1. Schematic drawing of cylindrical bars fabricated by EBM.

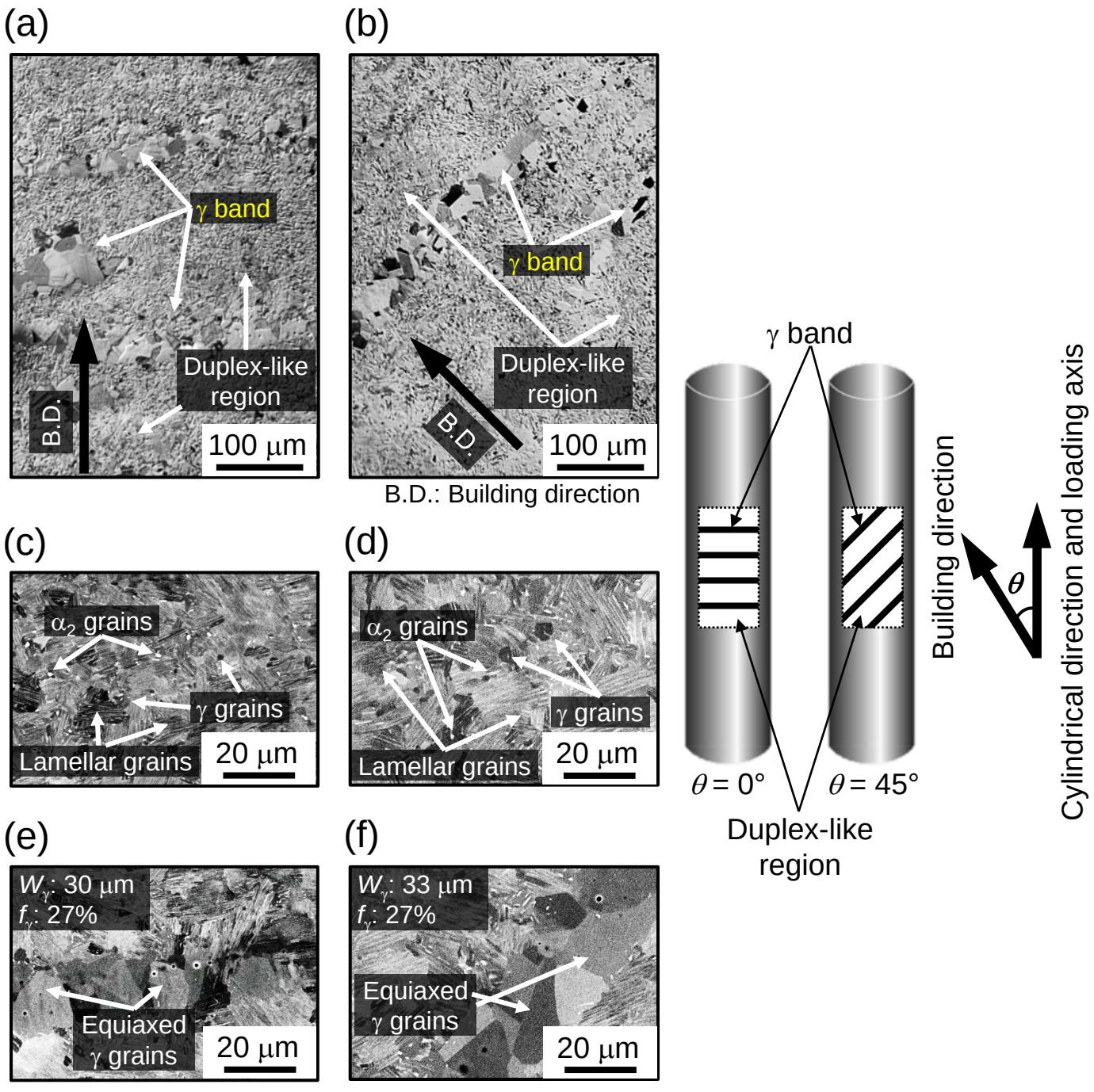

Fig. 2. OM and SEM images of $\theta = 0^{\circ}$ ((a), (c), (e)) and $\theta = 45^{\circ}$ ((b), (d), (f)); OM images ((a), (b)), SEM images of the duplex-like region ((c), (d)) and the γ band ((e), (f)).

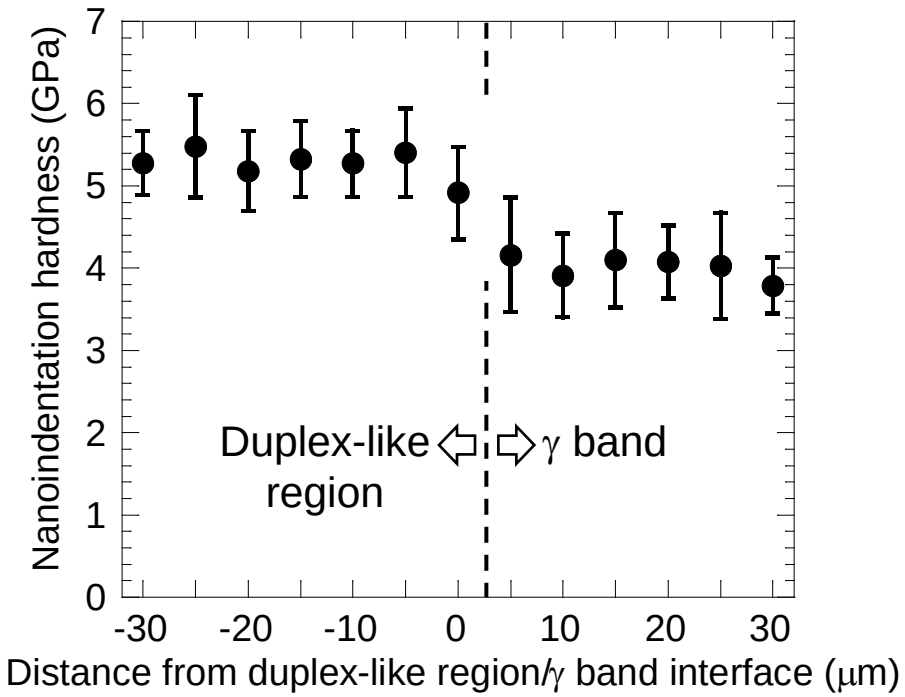

Fig. 3. Nanoindentation hardness distribution in $\theta = 0^{\circ}$, measured near the duplex-like region/γ band interface.

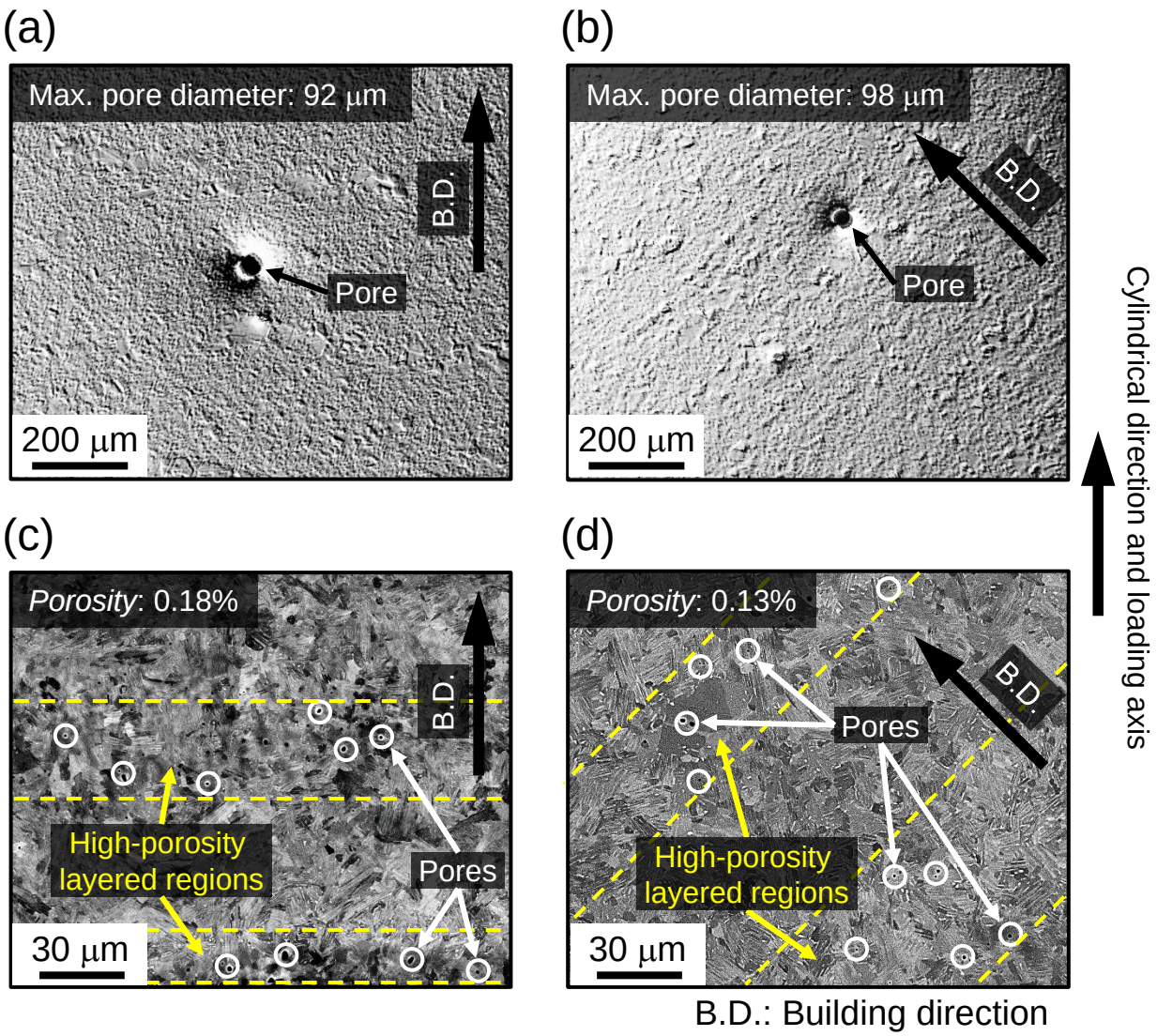

Fig. 4. OM ((a), (b)) and SEM ((c), (d)) images of pores in $\theta = 0^{\circ}$ ((a), (c)) and $\theta = 45^{\circ}$ ((b), (d)).

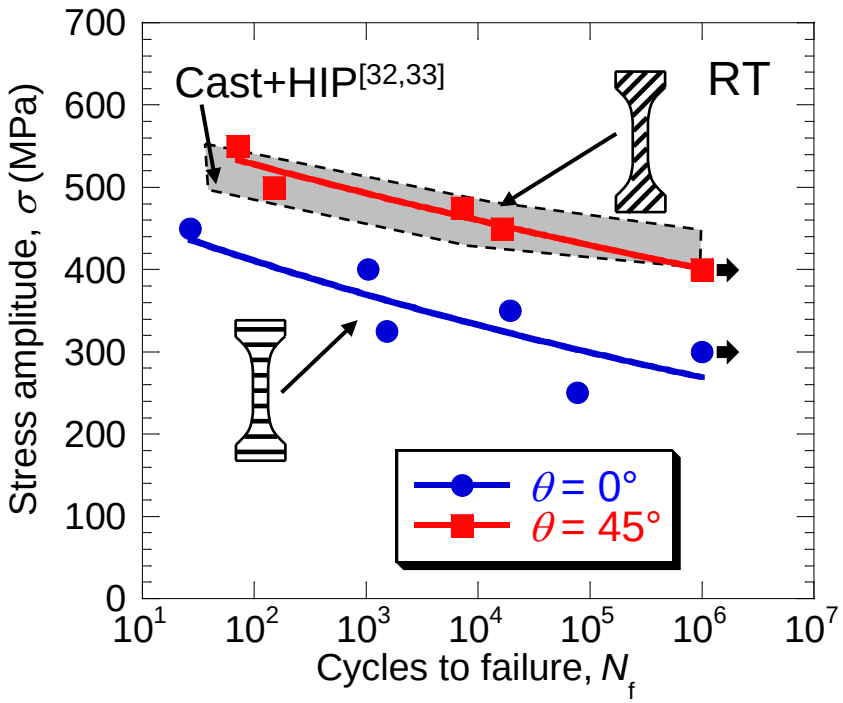

Fig. 5. S-N_f curves of $\theta = 0°$ and $\theta = 45°$ cyclically deformed at RT, along with that of the cast alloys with HIP treatment.

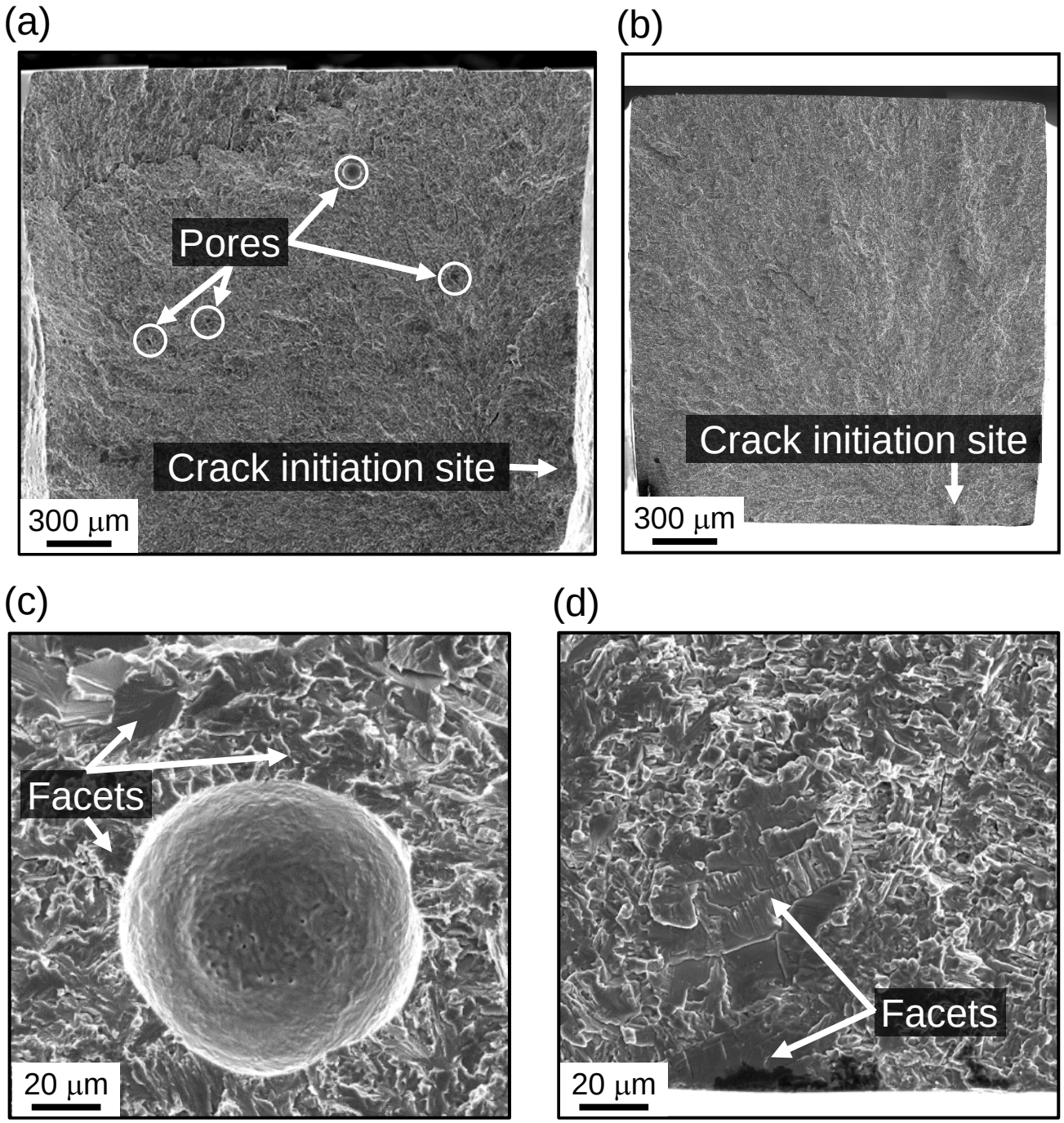

Fig. 6. SEM fractographs after the fatigue tests at RT. (a), (c) $\theta = 0^\circ$, σ = 400 MPa, N_f = 1042 cycles, (b), (d) $\theta = 45^\circ$, σ = 500 MPa, N_f = 151 cycles. (a), (b) Low magnification images of the fracture surface, (c) a pore surrounded by some facets, (d) crack initiation site of near the specimen surface.

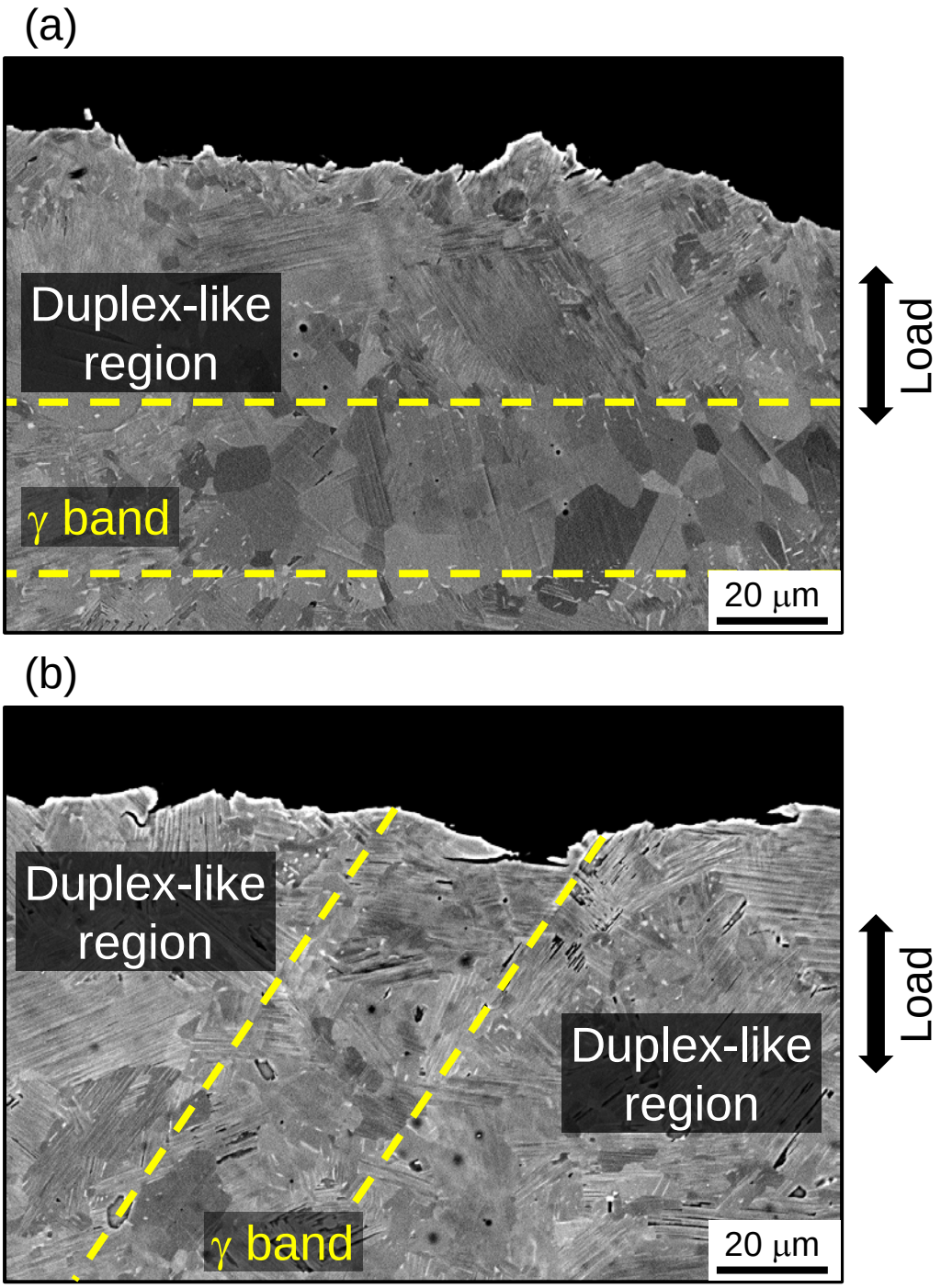

Fig. 7. Side view SEM images of fracture parts after the fatigue tests at RT. (a) $\theta = 0^{\circ}$, σ = 400 MPa, N_f = 1042 cycles, (b) $\theta = 45^{\circ}$, σ = 450 MPa, N_f = 16378 cycles.

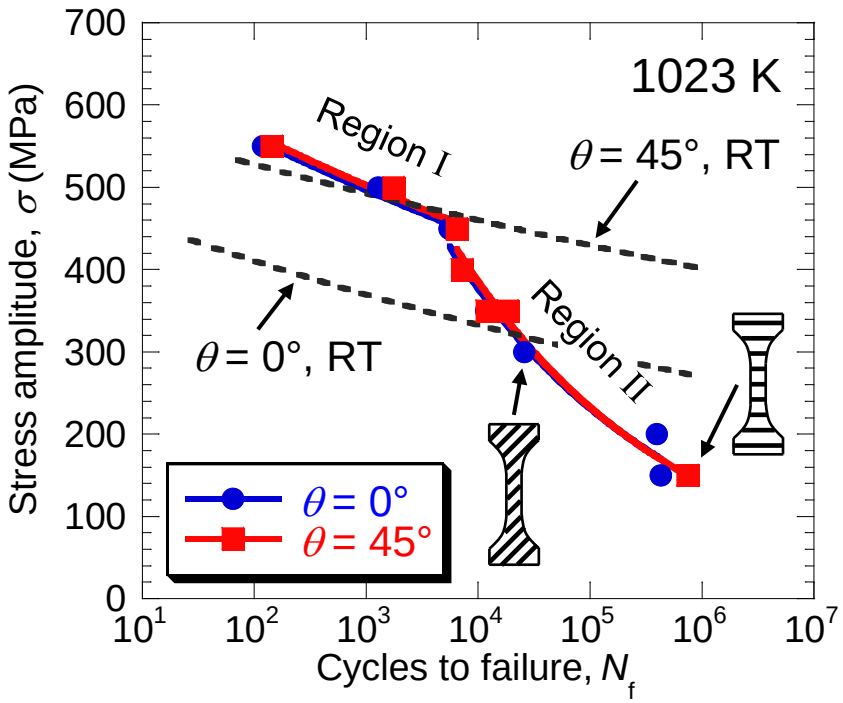

Fig. 8. S-N_f curves of $\theta = 0^\circ$ and $\theta = 45^\circ$ cyclically deformed at 1023 K, along with those at RT.

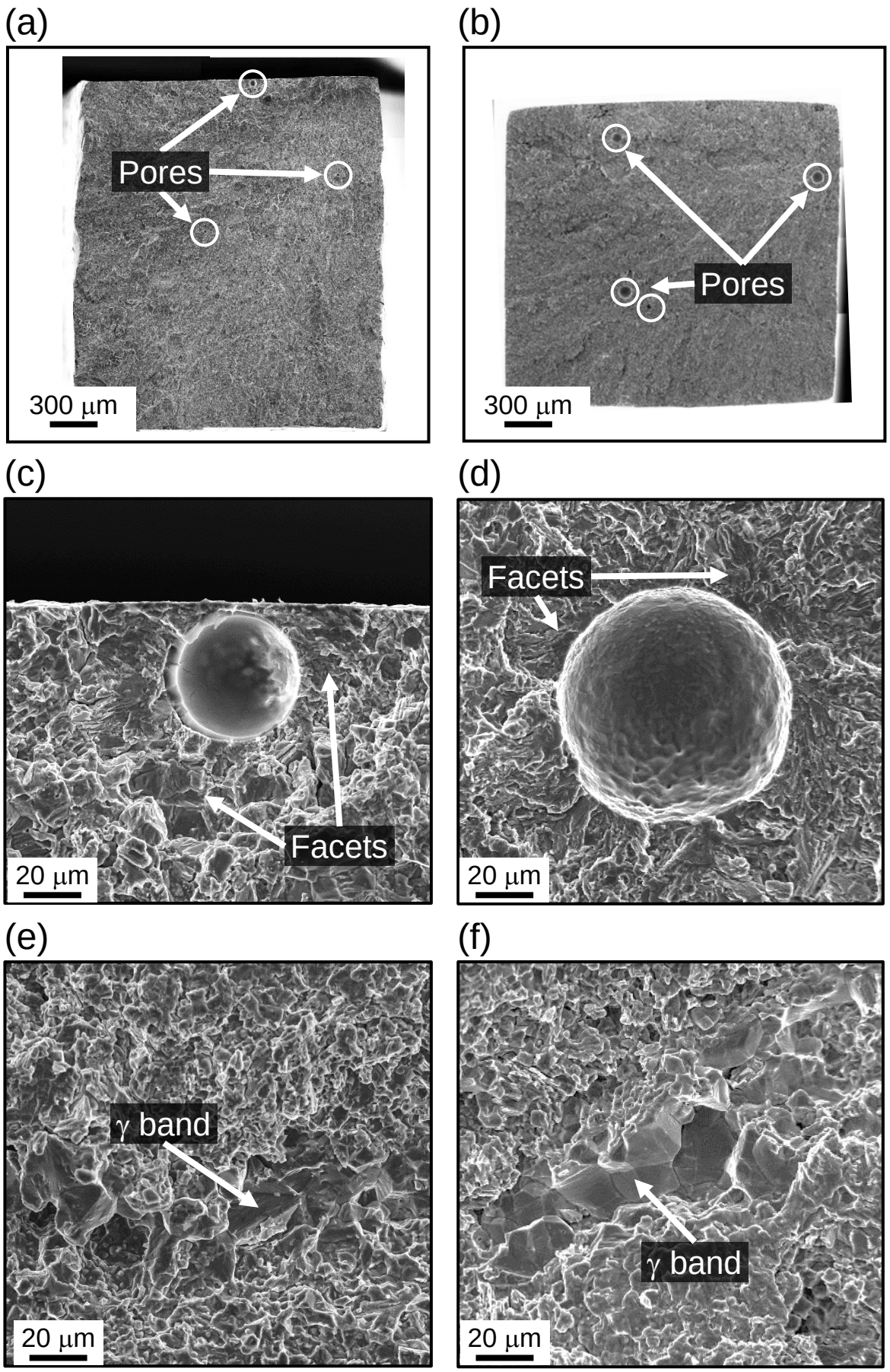

Fig. 9. SEM fractographs after the fatigue tests at 1023 K. (a), (c), (e) $\theta = 0^\circ$, $\sigma = 350$ MPa, $N_f = 11748$ cycles, (b), (d), (f) $\theta = 45^\circ$, $\sigma = 350$ MPa, $N_f = 11903$ cycles. (a), (b) Low magnification images of the fracture surface. The pores ((c), (d)) and the γ bands ((e), (f)) observed on the fracture surface.

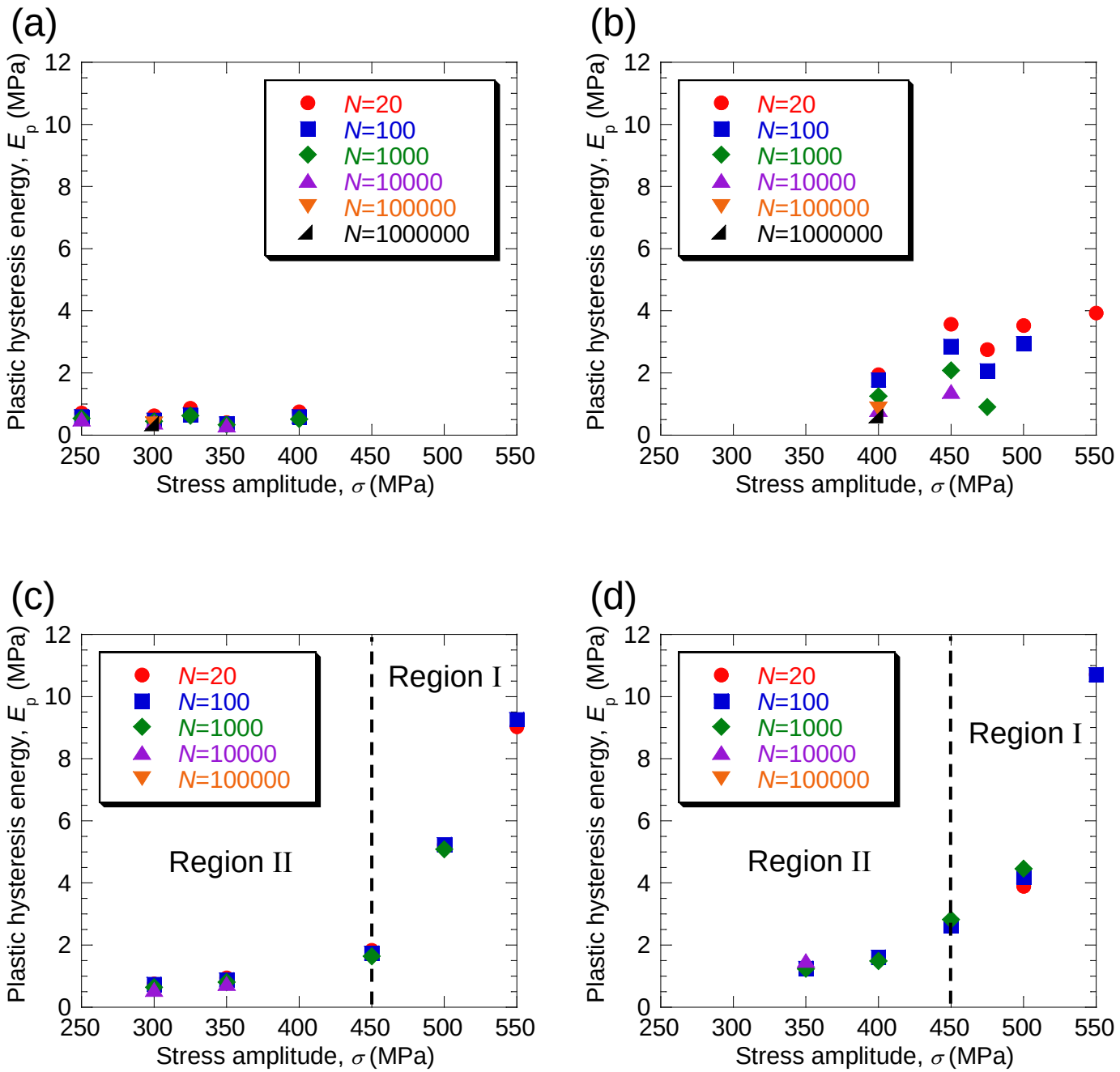

Fig. 10. Variation in E_p with σ for $\theta = 0^\circ$ ((a), (c)) and $\theta = 45^\circ$ ((b), (d)) at RT ((a), (b)) and 1023 K ((c), (d)).

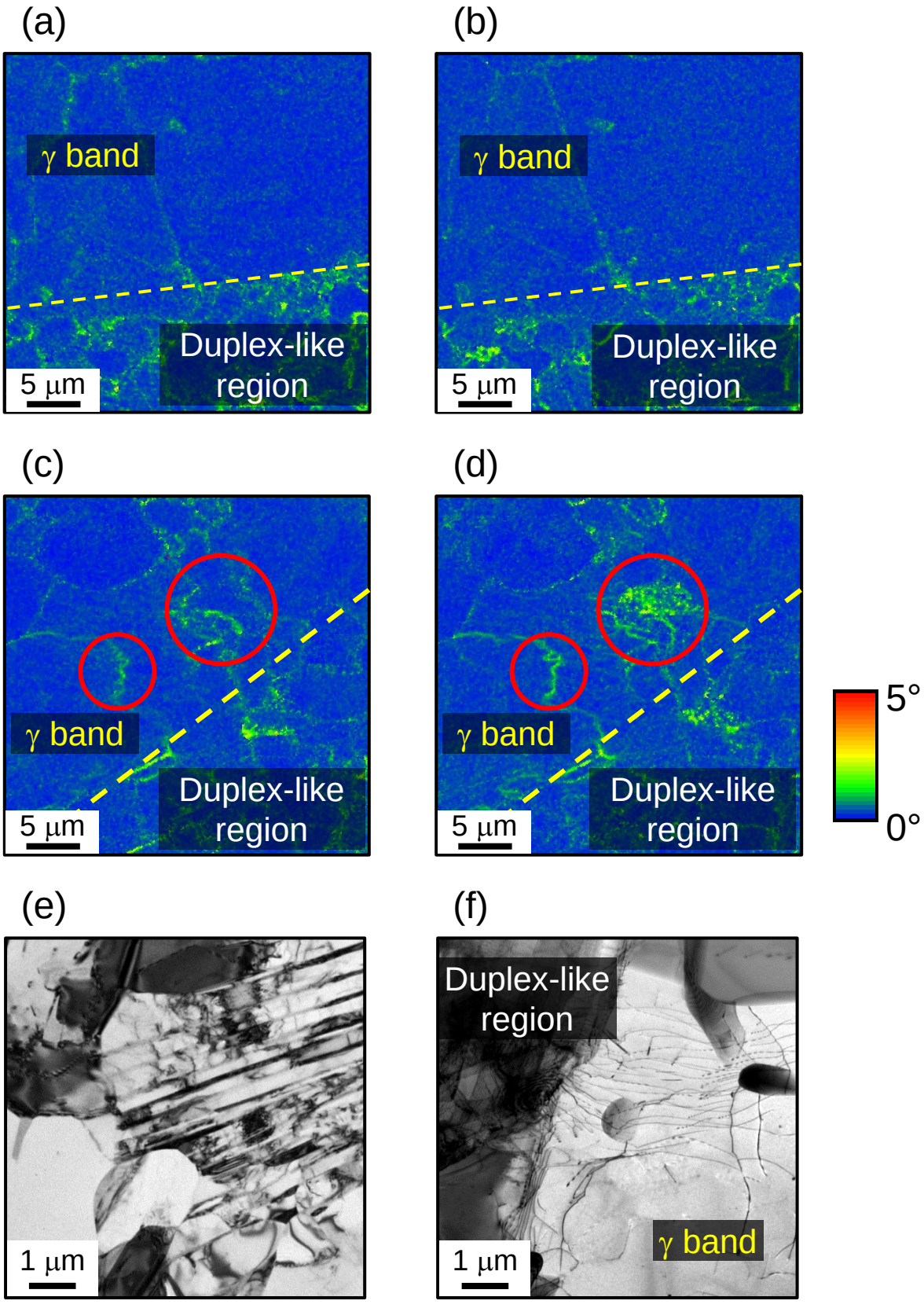

Fig. 11. EBSD KAM maps of $\theta = 0^\circ$ ((a), (b)) and $\theta = 45^\circ$ ((c), (d)) before ((a), (c)) and after ((b), (d)) the fatigue tests at RT; $\sigma =$ 300 MPa, $N = 1 \times 10^5$ cycles. (e), (f) TEM bright-field images of dislocation structure in fatigued $\theta = 45^\circ$. (e) The duplex-like region, (f) the duplex-like region/γ band interface.

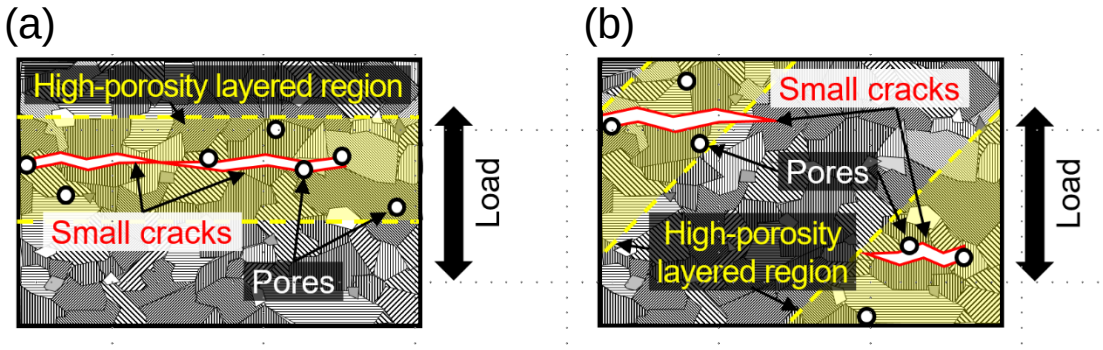

Fig. 12. Schematic drawing of small crack propagation at $\theta = 0^\circ$ (a) and $\theta = 45^\circ$ (b). Unlike in the case of $\theta = 0^\circ$, small cracks cannot easily connect with each other and propagate in $\theta = 45^\circ$.

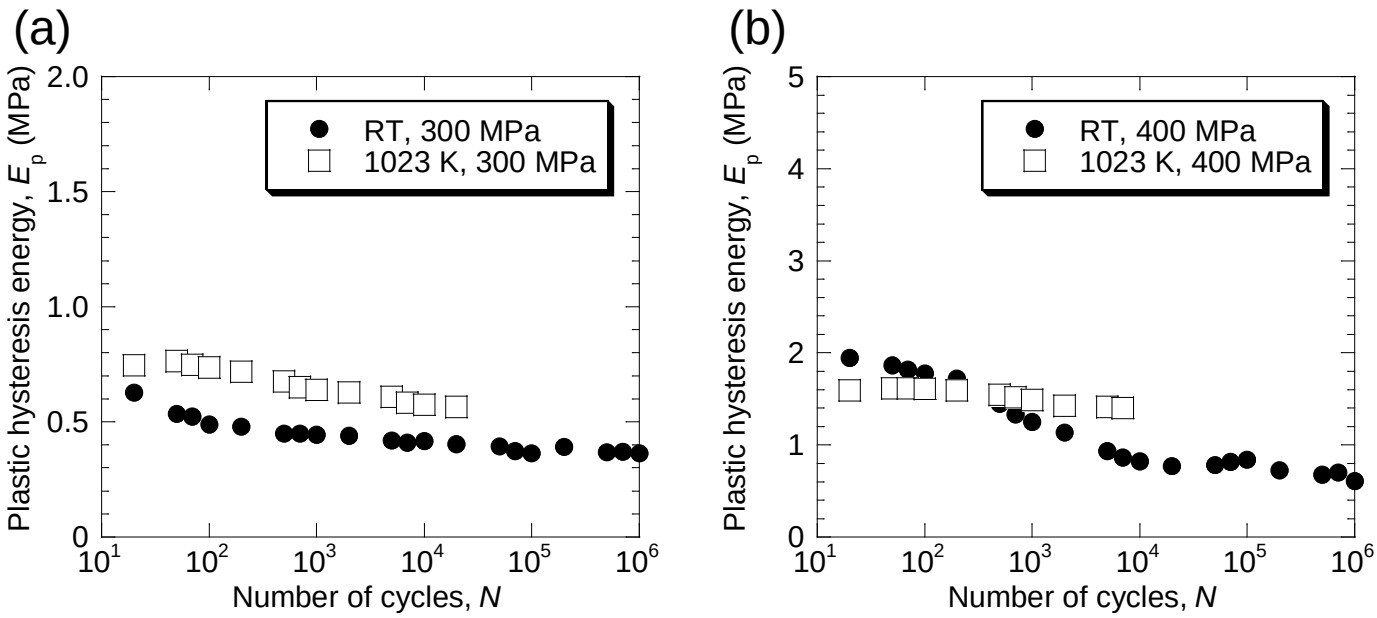

Fig. 13. Variation in E_p with N for $\theta = 0^\circ$ (a) and $\theta = 45^\circ$ (b) fatigue tested at RT or 1023 K. (a) $\sigma = 300$ MPa, (b) $\sigma = 400$ MPa.